京都大学防災研究所年報 第 65 号 B
DPRI Annuals, No. 65 B, 2022

Fundamental Research on Water Vapor Inflow Path into the Back-building Convective System and its Relationship with Atmospheric Stability

Yukari NAKA, Taiga KAMIYA(1) and Eiichi NAKAKITA

仲ゆかり・神谷太雅(1)・中北英一

(1) Dept. of Civil and Earth Resources Eng., Kyoto University

Synopsis

In the Baiu season, heavy rainfall often occurs and has caused a lot of damage in Japan. In this research, since the supply of water vapor is essential for the back-building convective system to occur and be maintained, the water vapor inflow path to the heavy rainfall area along terrain was focused on the meso-α~β-scale. Indeed, such a water vapor inflow path can be confirmed by three-dimensional water vapor flux in this research. Moreover, since atmospheric stability which is changing due to global warming can change the flow, a hypothesis that atmospheric stability can affect the water vapor inflow stability condition was changed with the reproductive experiment. As a result, if the atmospheric condition is more stable, water vapor flux gradually becomes thinner and higher due to the stronger convergence along terrain, and the total inflow of water vapor flux is also increased slightly. In addition, the tendency that such amplifying of the water vapor flux happens under more stable conditions was confirmed in the past real cases by the clustering classification of the past cases.

Keywords: Back-building convective system, water vapor inflow path, atmospheric stability, global warming, water vapor flux, Baiu season

1. Introduction

1.1 Background

In Japan, a lot of damage has been caused by heavy rainfall from June to July every year. In Japanese, this period is called “Baiu” season, and heavy rainfall often occurs during the season (hereinafter referred to as Baiu heavy rainfall). The large convergence zone appears as the Baiu front, and the so-called back-building convective system often occurs in the zone, which is considered the typical type of Baiu heavy rainfall. It brings localized and sudden heavy rainfall and stagnates for several hours, therefore it induces floodings in small and medium river basins and landslides, then have often caused a lot of property damage and human suffering.

Baiu heavy rainfall is a phenomenon caused by a hierarchy of mechanisms in multi-scales (Ninomiya, 1984), but it is difficult to generate and maintain without the presence of water vapor. In the Baiu season, the Baiu frontal zone exists as a convergence zone which is a significant subtropical front in East Asia. It is the area where the gradient of the equivalent potential temperature θ_e and the gradient of water vapor mixing ratio q_v are both strong due to the conflict of different air masses, and where convective instability generates frequently with a large moisture flux convergences and a significant upward motion (Ninomiya, 1984). In

addition, the strong low-level convergence of warm and humid air containing abundant water vapor into the frontal zone is associated with the advection in the western periphery of the Pacific anticyclone, which is considered a meso-α-scale phenomenon (Ninomiya and Akiyama, 1992). Additionally, such a largescale inflow of warm and humid air splits up or branches due to some factors such as the topography and atmospheric environment and enters and penetrates the inner land area bringing a lot of water vapor (meso-α~β-scale). Thus, due to this abundant supply of water vapor, it becomes a condition that heavy rainfall is more likely to occur, such as a decline of the level of free convection and the rise of the level of neutral buoyancy for cumulonimbus (Yoshizaki and Kato, 2007). Lastly, by some triggers in meso-γ-scale, cumulonimbus successively occurs, for example, due to the convergence field caused by mountains (Nakakita et al., 1988; Yokota, 1992). Then, the back-building convective system consists of multiple self-organized cumulonimbi in a linear structure. Convective cells generated successively upstream of the system move downstream along the mid-level wind and merge into the system. This process is cyclically repeated while the convective system is developing, hence the system forms a line-shaped structure and stagnates and stays in place. Although individual convective cells repeat development and then decline, the system is maintained and stationary as a whole precipitation system. Thus, it forms a line-shaped structure and stagnates in place, so which brings localized heavy rainfall for a period from several hours to half a day.

Therefore, the water vapor inflow is essential for both the generation and maintenance of Baiu heavy rainfall since the process that brings a heavy rainfall as is mentioned cannot occur without water vapor inflow.

However, although many studies have focused on Baiu heavy rainfall in multi-scales, the process by which the water vapor flow splits and enters the land area (water vapor flow along topography), which is the connection between the phenomena of meso-α-scale and meso-β-scale, has not been clarified in detail. On the other hand, in fact, by checking the amount of precipitation of some past heavy rainfall events, the supply route of water vapor to the heavy rainfall area along topography can be estimated in meso-α~β-scale as is shown in Fig. 1. Therefore, the unclear point how water vapor flows over land along the topography is still a matter of debate. Clarification of this point could lead to a better understanding of the mechanism of occurrence and development of heavy rainfall in the Baiu season and could contribute to improved forecast accuracy.

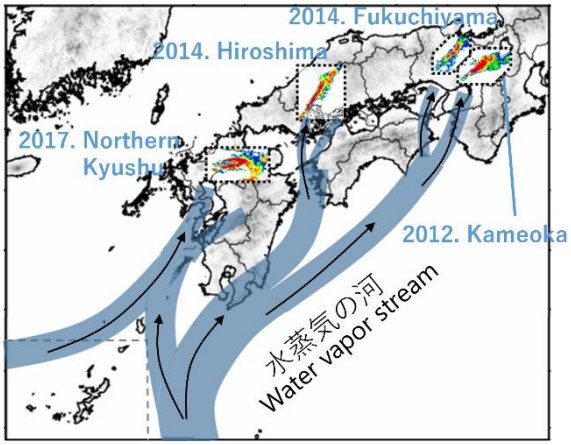

Fig. 1 the accumulation of past local Baiu heavy rainfalls seen in XRAIN and the conceptual diagram of the water vapor path.

Furthermore, in considering the Baiu heavy rainfall, it is necessary to discuss the impact of global warming. Some studies have revealed that the intensity and frequency of the Baiu heavy rainfall increase due to global warming by future climate experiments based on a scenario of a 4℃ rise in global average temperature, RCP8.5 (Osakada and Nakakita, 2018). The results showed a 5% significant increase in heavy rainy season rainfall in early July, early and mid-August in the future climate, and an increase by region in northern Japan and the Sea of Japan, including Hokkaido, Tohoku, Hokuriku, and Chugoku regions. Moreover, a pseudo-global warming experiment on the Kameoka heavy rainfall event which is classified as a back-building heavy rainfall in the Baiu season revealed that rainfall intensity and total rainfall increase in the future (Nakakita and Osakada, 2020). Moreover, it revealed that such a result was induced by the increase in the amount of condensation in cumulus clouds, the realization of a convective instability field, strengthening of the structure of the linear

convection system itself, and continuous supply of convective instability air from the south.

In addition, in the future climate in which global warming proceeds, atmospheric stability which can change the flow of fluid is said to be more stable. In unstable conditions, when fluid is flowing toward an object, the fluid tends to flow over the object to pass it, as is illustrated in Fig. 2. On the contrary, in stable conditions where global warming is occurring, the fluid does not try to flow vertically, but tries to go around horizontally to pass through the object, as illustrated in Fig. 3. Thus, since there is a potential impact on flow by atmospheric stability, it is necessary to discuss the changes in the Baiu season in the future climate due to global warming, taking into account the changes in atmospheric stability. This perspective could help us better understand the changes in Baiu season rainfall that are becoming more intense and frequent due to global warming.

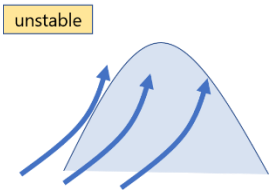

Fig. 2 flow in unstable conditions.

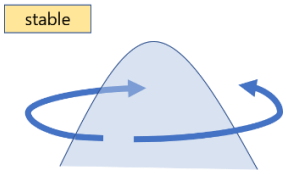

Fig. 3 flow in stable conditions.

1.2 Objectives

As mentioned above, the water vapor inflow is essential for the existence of heavy rainfall in the Baiu season. Although many studies on the Baiu heavy rainfall have been conducted with multi-scale analysis, it still exists unknown to resolve and has not been performed the analysis regarding the meso-α~β-scale water vapor inflow along the terrain in the Baiu season. Therefore, in this research, it is confirmed if the supply of water vapor along topography existed in some past heavy rainfall events by using the Grid Point Value (GPV) of the Meso-Scale Model (abbreviated as MSM hereafter) to investigate how water vapor inflow is important for Baiu heavy rainfall and to clarify whether there is water vapor inflow path like Fig. 1.

Moreover, there is a necessity to discuss the impact of global warming on Baiu rainfall. Therefore, this study focuses on atmospheric stability which is changing as global warming is processed. Since it is not yet known how water vapor inflow paths are defined, this study first focuses on how atmospheric stability affects water vapor flow as a fundamental study. To elucidate the relationship between atmospheric stability and water vapor inflow, some sensitivity experiments in which the stability is changed are conducted by using the Cloud Resolving Storm Simulator (CReSS), which is the cloud-resolving, non-hydrostatic, quasi-compressible mesoscale atmospheric model for accurately simulating mesoscale phenomena, and the results are compared with each other to test the hypothesis discussed below.

In addition, clustering analysis using the Self-Organizing Map (abbreviated as SOM hereafter) is conducted to investigate the relationship between the stability and the water vapor inflow using real-world observed values.

The proposed research can help understand the universal mechanism relating to stability and water vapor inflow into the back-building convective system in the Baiu season and also useful when considering the future changes due to global warming.

1.3 Hypothesis

In this paper, a hypothesis was formed regarding the relationship between atmospheric stability and the way water vapor flows along the topography.

First of all, generally, from the viewpoint of fluid dynamics, when fluid is flowing toward an object, the fluid tends to flow vertically to pass over the object in unstable conditions. On the contrary, in stable conditions, the fluid is more likely to move horizontally to go around and pass through it.

According to the conventional understanding and observations concerning atmospheric stability, it is natural to conjecture that atmospheric stability influences the path of water vapor inflow as the dynamical field and the motion of the thermodynamic flow. In detail, in unstable conditions, it is likely that the flow of water vapor would be elevated by the terrain, as is shown in Fig. 4(a). Conversely, in highly stable conditions, air mass containing water vapor would likely go along the topography and easily converge in the direction of narrowing terrain to pass through the terrain. Owing to this effect, the flow would get stronger

along the terrain and gather water vapor, then water vapor assembles more in the lower layer, and such the water vapor flow merged would be elevated to mid-level, as is illustrated in Fig. 4(b).

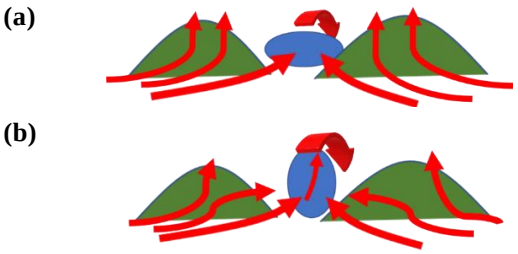

Fig. 4 Hypothetical diagram of water vapor flow (a) in unstable conditions and (b) in stable conditions.

To verify the hypothesis and to better understand the relationship between atmospheric stability and water vapor flow, sensitivity experiments with stable atmospheric conditions were performed with numerical simulations CReSS, and the clustering classification of the past atmospheric data was carried out to confirm whether the results of sensitivity experiments can be seen in real atmospheric fields.

2. Analysis of water vapor inflow paths in past cases of Baiu heavy rainfall

This chapter presents the results of analysis utilizing MSM of how the path of water vapor inflow can be identified in past cases of heavy rainfall. To grasp the characteristics of how the water vapor flowed into the rainfall area in some past heavy rainfall cases and to confirm if the water vapor was supplied to the heavy rainfall area like Fig. 1, the MSM data was analyzed from a slightly larger perspective of spatial scale (meso-α~β-scale) by focusing on the flow of water vapor along the terrain around the Kii and Bungo channel.

2.1 Data for analysis

In this chapter, the objective analysis data of the MSM was used. MSM is the meso-scale numerical meteorological model of the Japan Meteorological Agency for numerical weather prediction. By MSM, the forecasting value of weather for the next 16 hours is outputted for every one hour by calculating from the initial value of the atmospheric conditions. Then, the forecasting value is then assimilated with the observation value every three hours. This assimilated value is called the MSM analysis value and was used in this research. The data in this analysis is denoted as MSM analysis data hereafter. MSM outputs data for the ground surface and 16 pressure levels, including 1000, 975, 950, 925, 900, 850, 800, 700, 600, 500, 400, 300, 250, 200, 150, and 100hPa. The spatial resolution of MSM is 5km for the ground surface and 10km for the pressure 10 levels.

In addition, to know the location and appearance of rainfall and correspond it to atmospheric conditions, the rainfall information observed by eXtended RAdar Information Network (well-known as XRAIN in Japan) is used. XRAIN is installed by the Ministry of Land, Infrastructure, Transport, and Tourism and consists of many X-band polarimetric doppler radars and C-band polarimetric radars to cover a fairly large area of Japan, mainly in major urban areas. XRAIN has a 250m spatial resolution and can output the data of surface composited rainfall every one minute. XRAIN is capable to evaluate rainfall quantitatively in very high resolution.

2.2 Target Events for analysis

The analysis in this chapter is focused on three past heavy rainfall events that are considered to have a water vapor inflow path, as is shown in Fig. 1. The first past event is Kameoka rainfall occurred in the period from about 00:00 to 06:00 JST (i.e., Japan Standard Time) on July 15th in 2012. Kameoka is located in the Midwest of Kyoto prefecture. The second case is Hiroshima rainfall that occurred in the period from about 00:00 to 04:00 JST on August 20th in 2014. Hiroshima rainfall occurred in accompany by the influence of the autumn stationary front of Japan instead of the Baiu front. Owing to the autumn stationary front, back-building convective systems often happen like in the Baiu season, therefore, Hiroshima rainfall is also analyzed in this research. The last event is Fukuchiyama rainfall, which occurred in the northern Kyoto prefecture. The reason why the Fukuchiyama rainfall was chosen is that it may have a similar inflow path of water vapor as the one in the Kameoka case such as

the inflow path originated from the Kii channel, however, the difference in the location of heavy rainfall would be due to a branching of water vapor path starting from Awaji Island as shown in Fig. 1. Therefore, the importance of the inflow path of water vapor could be highlighted by comparing the Kameoka and Fukuchiyama cases.

2.3 Indicators used for comparison

The characteristics of the three aforementioned events are analyzed and compared with each other by utilizing five indices obtained from MSM analysis data, including 1) surface wind, 2) surface water vapor mixing ratio, 3) surface water vapor flux, 4) CAPE and 5) vertical profile of the inflow amount of water vapor flux.

(1) Explanation of CAPE

CAPE (convective available potential energy), of which the unit of [J/kg], is one of the indices representing the instability of the atmosphere, and is defined as the integration of the buoyancy working on elevating an air parcel from LFC (level of free convection) to EL (equilibrium level), i.e.,

$$CAPE = \int_{LFC}^{EL} g \frac{T(z) - \bar{T}(z)}{\bar{T}(z)} dz, \qquad (1)$$

where z is altitude, $T(z)$ is the temperature of the air parcel, $\bar{T}(z)$ is the temperature of the surrounding, and g is the gravitational acceleration. A higher value of CAPE means that the atmosphere is more unstable with a high potential to produce a stronger updraft and more energy for inducing the convection. In addition, CAPE becomes higher when the lower layer gets more moisture.

(2) Method for understanding the vertical structure of water vapor inflow

To capture the water vapor path in three dimensions and to examine differences in the structure of water vapor inflow including a vertical direction, the vertical profile of the amount of water vapor flux was examined as follows. Firstly, set rectangular ranges surrounding the target channels, which are considered to be the path for water vapor, as illustrated in Fig. 5. Secondly, calculate the accumulation of water vapor flux flowing into the constant parallel lines for every 0.1 degrees for each pressure level, that is, the flux for each pressure level is expressed as

$$F_{total} = \int_{\phi_w}^{\phi_e} F(x)dx\,, \qquad (2)$$

where ϕ_e and ϕ_w are the longitudes of east and west borders of the range, respectively, and F is the water vapor flux on each grid at the constant latitudes. The northward direction is defined as positive. The flux amount is calculated as the magnitude of the vector. Lastly, plot it with the geopotential height obtained for each pressure surface to get the vertical profile of water vapor flux. The south-north vertical cross-section which shows the water vapor flux towards the north with integration in the east-west direction is acquired through this procedure.

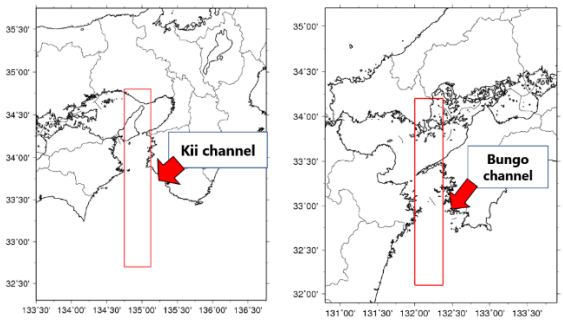

(a) Target region for Kameoka and Fukuchiyama rainfall around the Kii channel

(b) Target region for Hiroshim rainfall around the Bungo channel

Fig. 5 The analysis range around the channels to investigate inflow of water vapor flux.

2.4 Comparison among the heavy rainfall events

By checking the flow motion retrieved by each index extracted from MSM analysis data, it was attempted to clarify the path of water vapor along topography. Consequently, the surface horizontal wind can show the flow well, however, it is difficult to determine whether a large amount of water vapor flowed into the rainfall area by using only the information of wind vectors. On the other hand, it is also difficult to understand where the flow was

coming from and going by only checking the value of the water vapor mixing ratio. On the contrary, surface water vapor flux can reveal the flow path of water vapor, and it flowed into the rainfall area. In addition, CAPE can also visualize the flow condition well and high CAPE inflowed into the rainfall area along topography. Therefore, this result suggests that surface water vapor flux and CAPE are capable of figuring out the flow of water vapor along the terrain from the south in the meso-α~β-scale.

Detailed behavior in each case is shown below.

(1) Kameoka heavy rainfall

During the rainfall, the water vapor flux flowed along the topography and flowed into the inside of the Kii channel, thus converged into the southwest tip of the rainfall area as shown in Fig. 6. The higher value of water vapor flux headed north from the eastern side of Awaji Island, which is considered as a junction of water vapor inflow from the south. Moreover, in accompanying by strong inflow, high CAPE is also distributed in the area inside the Kii channel during the rainfall event. The streams of high CAPE converged sharply (thin and spindly) and flowed towards the rainfall area as shown in Fig. 7.

Since the surface water vapor flux was found to flow into the heavy rainfall area and show the water vapor inflow path well, the three-dimensional inflow of water vapor flux including the vertical direction was examined to investigate differences in the structure of water vapor inflow. In the Kameoka case, the larger amount of water vapor flux flowing into the Kii channel can be found in the low level (lower than 2km height) during the rainfall rather than the time before and after rainfall, as is shown in Fig. 8. In addition, at around 33.7 degrees of latitude where the terrain narrows, it shows a higher value of water vapor flux that is possibly gathered by the narrowing topography of the Kii channel. Besides, the same analysis of the inflow amount of water vapor flux was also performed for the non-rainfall time. The

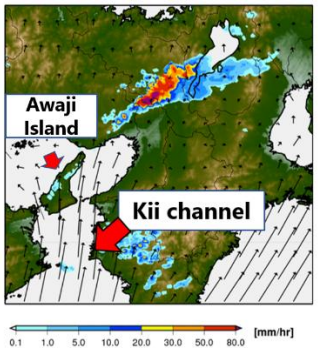

Fig. 6 Surface water vapor flux (arrows) obtained by MSM and rainrate obtained by XRAIN at 03:00JST on July 15th, 2012.

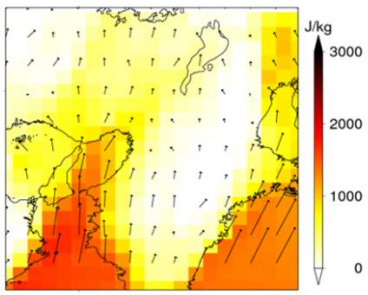

Fig. 7 Spatial distribution of CAPE (shade) and surface wind (arrows) obtained by MSM at 00:00JST on July 15th, 2012.

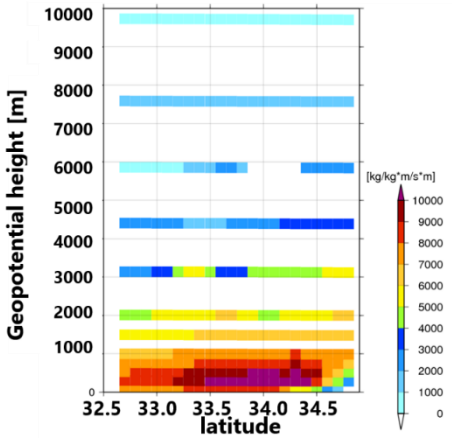

Fig. 8 Vertical distribution of the amount of water vapor flux inflowing along the Kii channel when the heavy rainfall happened (03:00 on July 15th, 2012) in south-north cross-section.

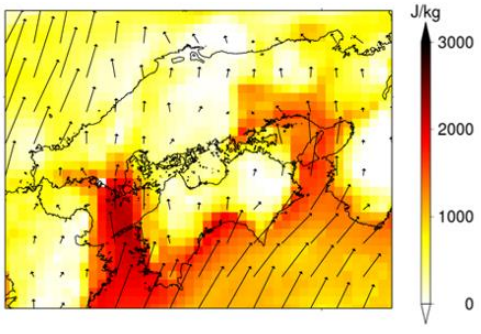

Fig.9 Spatial distribution of CAPE (shade) and surface wind (arrows) obtained by MSM at 03:00JST on August 20th, 2014. Heavy rainfall was happening in Hiroshima but not in the Kinki region.

time when Hiroshima rainfall occurred was used as an example of the non-rainfall time in the Kinki region. During this time, in accompanying by strong inflow, a high CAPE was also distributed over the Kii channel, as is shown in Fig. 9, but there existed no rainfall in the Kinki region. By calculating the amount of the inflow flux of water vapor, it is clear that the amount of water vapor flux is obviously less than that of Kameoka rainfall, as can be seen in Fig. 10. Therefore, this result reveals that the amount of water vapor flux definitely differs between the time of heavy rainfall and the time of non-rainfall, even though the inflow of high CAPE was found.

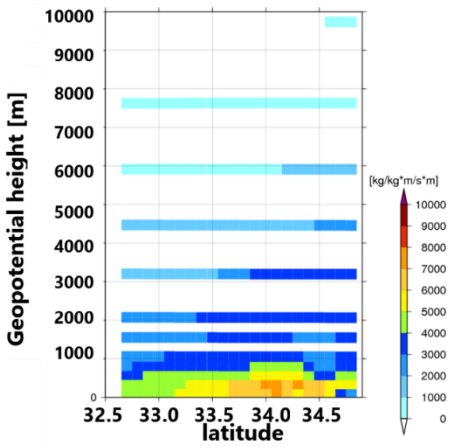

Fig. 10 Vertical distribution of the amount of water vapor flux inflowing along the Kii channel when the heavy rainfall did not happen (03:00JST on August 20th, 2014) in the south-north cross-section.

(2) Hiroshima heavy rainfall

In the similar condition of Kameoka rainfall, it can be found that water vapor flux flowed along the terrain and into the Bungo channel. Accordingly, the inflow of water vapor flux reaches the southwest tip of the heavy rainfall area, as is shown in Fig. 11. This feature can also be found in the previous research (Hibino et al. (2018)). Furthermore, in accompanying by strong inflow, high CAPE is also distributed over the Bungo channel and the high CAPE spatial distribution becomes sharp during rainfall, as is shown in Fig. 9.

The amount of water vapor flux flowing into the Bungo channel was examined at the heavy rainfall time and non-rainfall time as well. At the time of

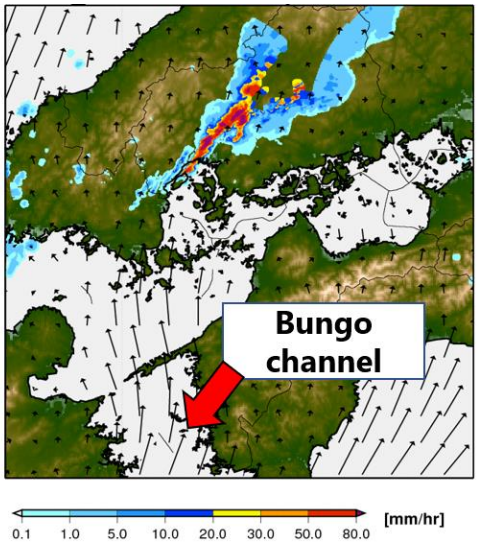

Fig. 11 Surface water vapor flux (arrows) obtained by MSM and rainrate obtained by XRAIN at 03:00JST on August 20th, 2014.

Hiroshima rainfall, a higher amount of water vapor appears in low-level during the rainfall rather than the time after the rainfall, as is shown in Fig. 12. In addition, the increment of the amount at the mid-level (2~4km) is also confirmed during the rainfall. Moreover, unlike in the Kameoka case, a larger amount of water vapor flux can be found before the rainfall. On the other hand, like the Kameoka case, at around 33.0 degrees of latitude where the terrain converges, it shows a larger amount of water vapor flux, which may possibly be gathered by the narrowing topography of the Bungo channel in the

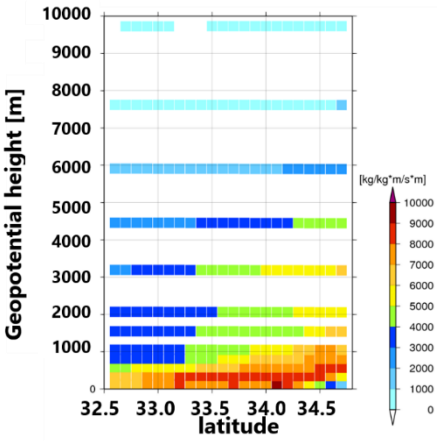

Fig. 12 Vertical distribution of the amount of water vapor flux inflowing along the Bungo channel when the heavy rainfall happened (03:00JST on August 20th, 2014) in the south-north cross-section.

same manner.

The amount of water vapor flux into the Bungo channel when the Kameoka rainfall happened was investigated as an example of the non-rainfall time of the area around Hiroshima. As is shown in Fig. 13, in the chosen period, high CAPE was distributed over the Bungo channel accompanied by strong inflow, however, there existed no rain around Hiroshima. As a result, in a similar condition of the case of the Kii channel during the non-rainfall time, the amount of water vapor flux at the non-rainfall time was much less than that of the heavy rainfall time. These differences can be found in Fig. 13.

(3) Fukuchiyama heavy rainfall

Again, in a similar condition to Kameoka rainfall,

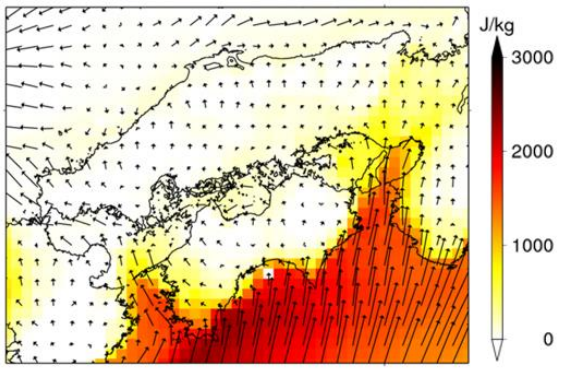

Fig.13 Spatial distribution of CAPE (shade) and surface wind (arrows) obtained by MSM at 00:00JST on July 15th, 2012. Heavy rainfall was happening at Kinki region but not around Hiroshima.

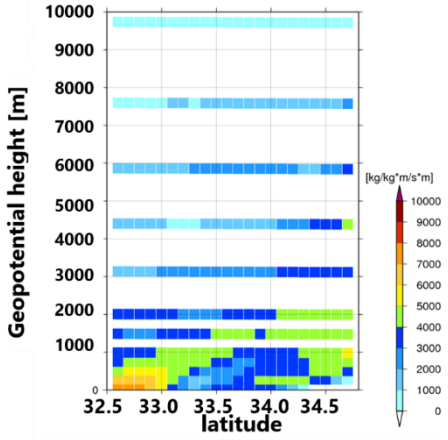

Fig. 14 Vertical distribution of the amount of water vapor flux inflowing along the Bungo channel when the heavy rainfall did not happen (00:00JST on July 15th, 2012) in the south-north cross-section.

the water vapor flux flowed along the topography and into the southern tip of the rainfall area. In addition, the water vapor came from the western edge of Awaji Island and over Awaji Island as shown in Fig. 15. Moreover, high CAPE can be found over Awaji Island as shown in Fig. 16, unlike the condition of Kameoka rainfall. Thus, as is expected that there would exist the inflow path of water vapor along the terrain as shown in Fig. 1, the difference in water vapor inflow path can be observed between Fukuchiyama rainfall and Kameoka rainfall events in terms of surface water vapor flux and CAPE.

2.5 Conclusion of Chapter 2

Through the analysis using the MSM analysis data, the paths of water vapor along the topography leading to the heavy rainfall area were identified in

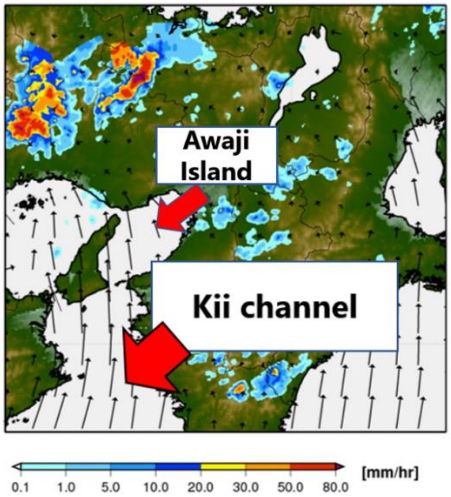

Fig. 15 Surface water vapor flux (arrows) obtained by MSM and rainrate obtained by XRAIN at 03:00JST on August 17th, 2014.

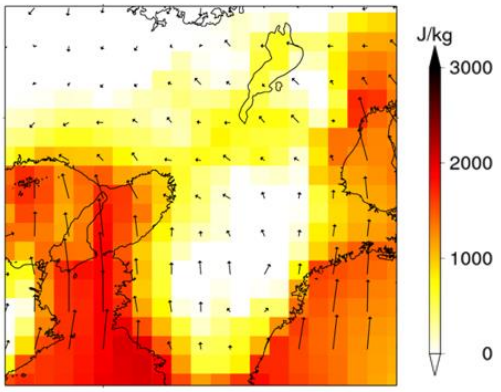

Fig. 16 Spatial distribution of CAPE (shade) and surface wind (arrows) obtained by MSM at 03:00JST on August 17th, 2014.

each historical case as expected. In each case, surface water vapor flux can visually reveal the path of inflow into heavy rainfall area well, such as pathways along the channels and those divided by Awaji Island. Thus, the horizontal distribution of water vapor flow along topography is important. In addition, CAPE can facilitate visualization of water vapor inflow to some extent, however, high CAPE with strong inflow is not a sufficient condition for the rain to occur. The reason why CAPE implies the flow well should be explored in future work. Simultaneously, by taking the vertical direction into account to examine the difference in water vapor flux, it is also verified that the larger amount of the inflow of water vapor flux into the channel at the rainfall time than at the non-rainfall time. This implies the importance of three-dimensional inflows of water vapor flux to comprehend the path of water vapor flow along with the topographical effect, and such inflow could be interpreted as a necessary condition for heavy rainfall.

3. Sensitivity experiments with different atmospheric conditions

In this paper, a reproductive experiment and two sensitivity experiments that assume more stable conditions than that of the reproductive experiment were performed using CReSS to analyze the effect of the atmospheric stability on water vapor inflow along the terrain. The reason why only the stable side is considered is that the basic understanding with a view to assessing the impacts associated with global warming is the objective of this study. The Kameoka heavy rainfall in 2012, was chosen as the target case because inflow along the terrain in the meso-α~β-scale was clearly seen by the last chapter's analysis.

3.1 Settings of Numerical experiments

(1) Settings of simulation

For the simulation experiments including both the reproductive and sensitivity experiments, the horizontal spatial resolution was set as 500 m and the vertical resolution was set to an average of 250m with stretching applied. MSM analysis data every 3 hours was utilized as the initial and boundary conditions of the experiments. The daily average of sea surface temperature supplied from NEAR-GOOS of the JMA was used as the boundary condition of sea surface temperature. The total simulation period is 9 hours which started at 21:00 JST on July 14th and ended at 06:00 JST on July 15th including the first 3 hours as a spin-up calculation time. The simulation region is the same as the region displayed in Fig. 17. In addition, all the detail of the experiment settings using CReSS are listed in Table 1.

(2) Settings for the stability conditions for sensitivity experiments

In order to check the impact of the atmospheric

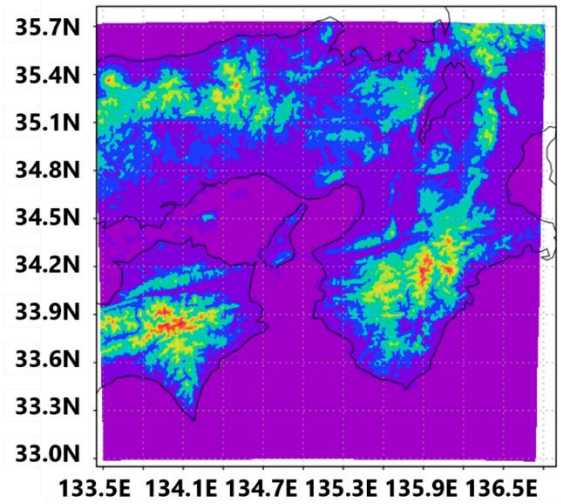

Fig. 17 Simulation range used in CReSS (shaded)

Table 1 Experimental settings of CReSS simulations

Resolution	Horizontal: 500m Vertical: 250m
Numbers of grid	Horizontal: 600×600 Vertical: 61 levels
Initial time	2012.07.14 21:00JST
Calculation time	9 hours
Initial & boundary data	The MSM analysis value
Sub-grid turbulence process	The 1.5 order closure with TKE
Cloud microphysics process	The bulk cold rain parameterization with solving tendency equation of number densities of ice phase hydrometeors

stability on the inflow of water vapor into the rainfall area, two sensitivity experiments that assume more stable conditions than that of the reproduction experiment were conducted.

To achieve more stable atmospheric conditions in the sensitivity experiments, the lapse rate was altered in the manner as follows. The temperature at 100 hPa was raised from the reproduction by 2℃ and 4℃ without changing the temperature at the surface to tilt the lapse rate. Between the surface and the pressure surface of 100 hPa, the difference in temperature from the reproduction was linearly interpolated. Hereinafter, for the sake of clarity, the reproductive and sensitivity experiments are defined as Exp (Rep), Exp (2), and Exp (4), respectively. For checking the difference in the stability, the slope of potential temperature $d\theta/dz$ is calculated linearly by using the values near the ground surface and around 5000 m of the initial value averaged in each experiment, and they are listed in Table 2. By these settings, Exp (Rep) has the most unstable, and Exp (2) and Exp (4) have almost the same stability conditions as the ones in RCP2.6 and RCP8.5 which assume 2 and 4℃ rise in global average temperature, respectively. Eventually, Exp (4) has the most stable condition.

3.2 Results of Numerical experiments

(1) Comparison in horizontal distribution of water vapor flow

The analysis was focused on investigating the difference in the way that wind flow at the ground surface. However, broadly speaking, contrary to the expectation that an obviously huge difference in the wind could be found through wind vectors between conditions of stability, differences were not seen to be significant in the speed and direction of the wind by only checking the horizontal distribution of wind vectors, as is shown in Fig. 18. The difference in the inflow of water vapor flux is also investigated near the ground surface by checking the spatial distribution of horizontal vectors, however, no obvious change in the direction and intensity of the vectors of water vapor flux was found through this approach. It is needed to determine the deviation from the mean and check for changes in flow in future work.

(2) Comparison of the vertical profile of water vapor flux

(a) Changes in south-north vertical cross-section of water vapor flux

Firstly, the analysis was focused on checking the amount of water vapor flux flowing northerly, which inflows into the Kameoka heavy rainfall area along the topography, in the vertical cross-sections in the south-north direction along the inflow path. To calculate the inflow of water vapor, first of all, the region for investigation was configured as the one which penetrates the heavy rainfall area (Kameoka area) along the inflow path which was confirmed in the analysis with MSM analysis data, like the red path in Fig. 19. Within this range, the water vapor

Table 2 The slope of $d\theta/dz$ calculated linearly between around 5000m to around the ground surface

	Reproduction Exp (Rep)	2℃ raised Exp (2)	4℃ raised Exp (4)
$d\theta/dz$	0.0048266	0.0049506	0.0050416

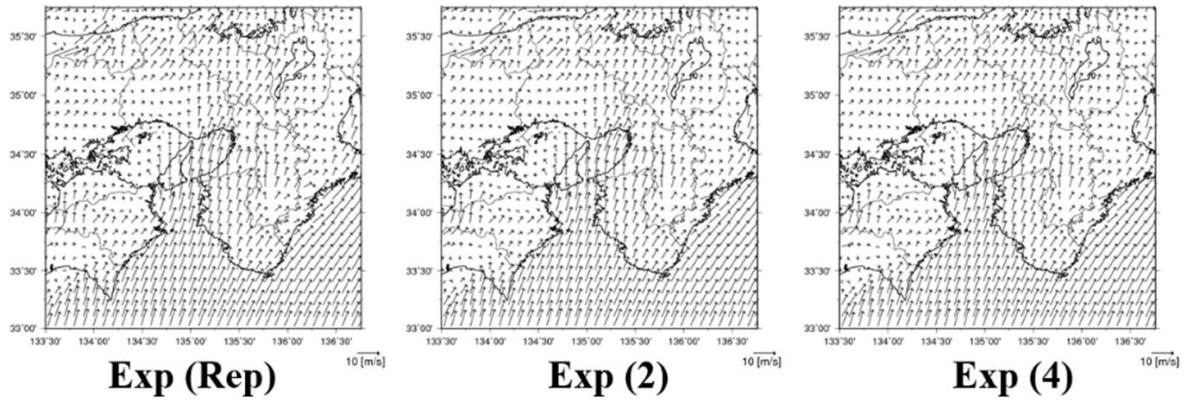

Fig. 18 Differences in surface wind flow among experiments at 00:25 on July 15th, 2012.

flux F,

$$F = q_v\sqrt{u^2 + v^2} * \frac{v}{|v|}, \qquad (3)$$

defined as positive towards the north was averaged hourly and averaged in the longitude direction for every 0.05 degree of latitude. This process is performed for each layer, and the vertical cross-sections of water vapor flux in the south-north direction along the topography from the Kii channel were obtained.

In all the rainfall periods of all experiments, the large amounts of water vapor flux in the low-level (below 2000 m) flowing northwardly can be found as seen in Fig. 20. This characteristic also can be considered a necessary condition for heavy rainfall as well as seen in the analysis with MSM concerning Kameoka rainfall and Hiroshima rainfall.

Furthermore, in the sensitivity experiments of Kameoka rainfall which have more stable conditions (Exp (2) and Exp (4)), after 01:00 JST, this low-level pool of large water vapor flux amplifies vertically at around 33.7 degrees of latitude where the Kii channel narrows, as illustrated in Fig. 20 (the figures of the time when a change was clearly seen are displayed). The more stable the atmospheric condition was, the stronger the low-level pool amplified vertically, which can be observed during the time from 02:00 to 05:00. This vertical bulge of water vapor flux implies that more water vapor flux converges together due to the stronger flow along the topography and it would be elevated in more stable conditions. From this perspective, the aforementioned hypothesis was formulated.

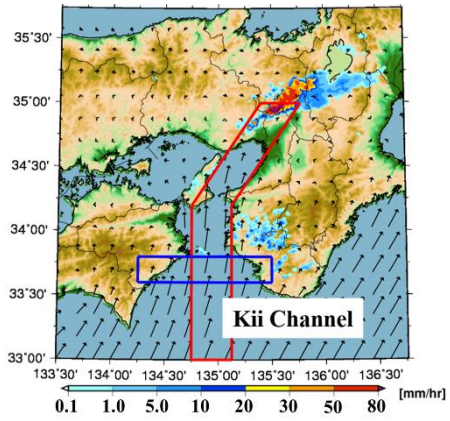

Fig. 19 Area set up to check the flow of water vapor flux along the terrain in the south-north direction (red frame) and set up to check it in the west-east cross-section (blue frame).

3.3 Verification of Hypothesis

To verify the hypothesis, in the application of the continuity equation, the following two analyses were conducted.

(1) Confirmation of the bulge of water vapor flux in the east-west cross-section

First, the inflow amount of water vapor flux into the east-west vertical cross-section at a constant latitude in the blue frame of Fig. 19 was checked because this region was where strong amplifying of water vapor flux happened. Moreover, only the part below 6000m where the bulge happened was focused on. In the domain, the amount of water vapor flux flowing northwardly was calculated by the length of vectors, and the hourly average was taken on each

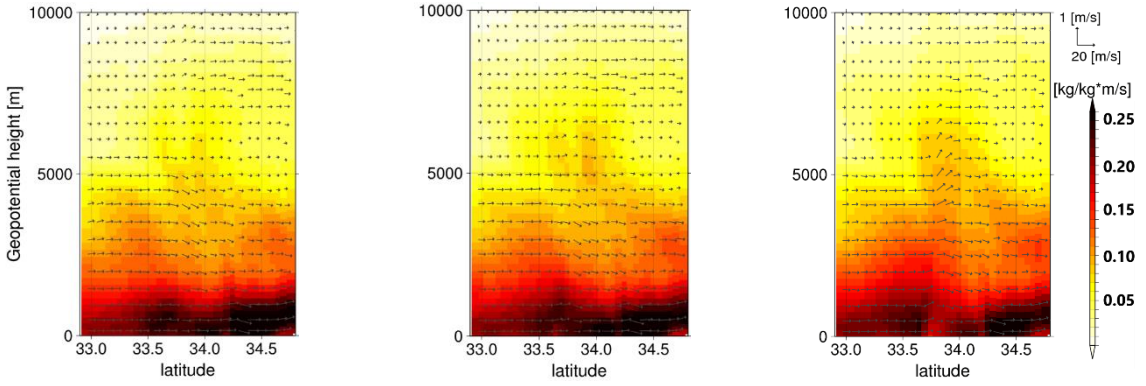

(a) Exp (Rep) (b) Exp (2) (c) Exp (4)

Fig. 20 Three-dimensional distribution of water vapor flux (shade) from 3:00 to 4:00 in the south-north vertical cross-section of the region framed in red in Fig.19 (x: latitude, y: altitude) and wind velocities (arrows) in each experiments.

grid. In the cross-sections, it is examined that the portions where the total amount of water vapor flux from the south is greater than the threshold are found to be equivalent in the west-east cross-section among experiments.

As is illustrated in Fig. 21, the threshold is firstly set (2 is used for simplicity in the explanation figure), and then it can be found that the area where the total amount of water vapor flux over the threshold is the same, of which the two areas circled by red lines in Fig. 21. Here, the threshold was set to be 0.09 kg/kg*m/s. Consequently, to obtain the same total amount of water vapor flux, the area should be like the area enclosed in gray in Fig.22. In short, the distribution of Exp (Rep) is wider and shorter than that of Exp (2). Also, the distribution of Exp (2) is wider and shorter than that of Exp (4). This result reflects that the inflow of water vapor flux gradually becomes thinner and higher under more stable conditions. This result is consistent with the physical manner considering the continuous equation. This kind of change between the conditions of atmospheric stability can be found by any threshold, therefore, the motions of amplified and slimmed water vapor flux can be considered as influenced by the variable conditions of atmospheric stability. Accordingly, under more stable conditions, around the Kii channel, the amplifying and slimming of water vapor flux happened as expected in the hypothesis.

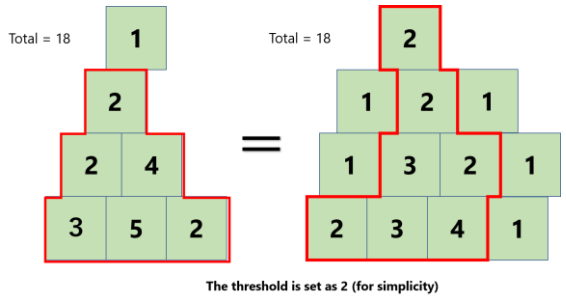

Fig. 21 Diagram explaining how to obtain the area where the total amount of water vapor flux is the same.

In addition, such amplifying under more stable conditions can also be found in the distribution of the water vapor mixing ratio. This result indicated that more water vapor is gathered into the area of the channel by the stronger flow along the terrain in more stable conditions. However, the amplifying was smaller than that of water vapor flux. It is because the flow of wind would also be gathered due to the stronger convergence caused by stronger flow along terrain under more stable conditions. Therefore, water vapor flux which is obtained by multiplying the water vapor mixing ratio and wind velocity can express the difference as amplifying better than only the water vapor mixing ratio.

(2) Verification to check differences in flow

Under more stable conditions, the inflow of water vapor flux into the Kii channel gradually became thinner and higher, since the flow along terrain would become stronger and gather more easily. To verify authenticity, the convergence in the x-direction is compared among the experiments in

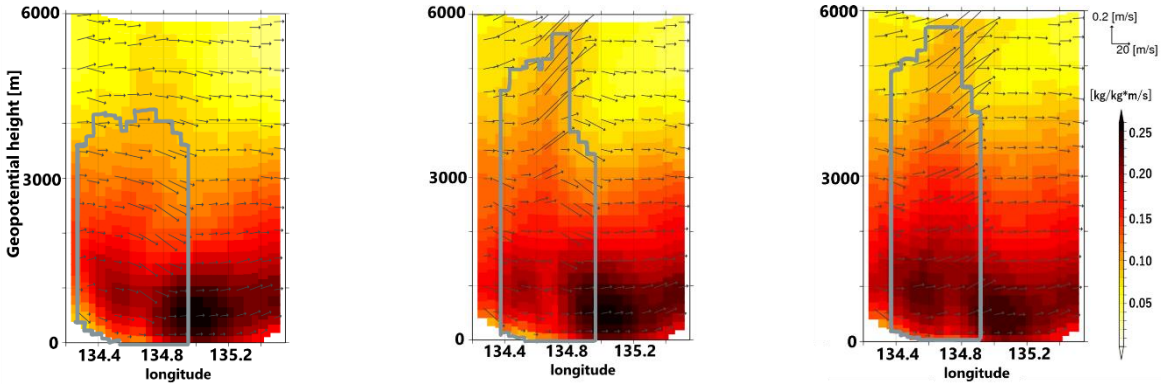

(a) Exp (Rep) (b) Exp (2) (c) Exp (4)

Fig. 22 Three-dimensional distribution of averaged water vapor flux (shade) from 3:00 to 4:00 in the west-east vertical cross-section of the region framed in blue in Fig.19 (*x*: longitude, *y*: altitude), gray frame represents the area where the total amount of water vapor flux is the same as Fig.21. Arrows corresponds to wind velocity.

this section.

The calculation region was set up around the inlet of the Kii channel, as Fig. 23, to avoid overlapping the land area. Within the region, the convergence of the *u*-component (m/s/m) is calculated

$$convergence = \sum_{height} \sum_{y} \frac{u_1 - u_2}{D}, \qquad (4)$$

where u_1 and u_2 are the wind speeds in the *x*-direction at the west and east boundaries, respectively, D is the width of the region, and the convergence is calculated by horizontally integrating along the *y*-axis, i.e., the boundaries of the region along the meridian and vertically along the axis of altitude, until the surface level of about 6000 m, where the last analysis concerning amplifying focused.

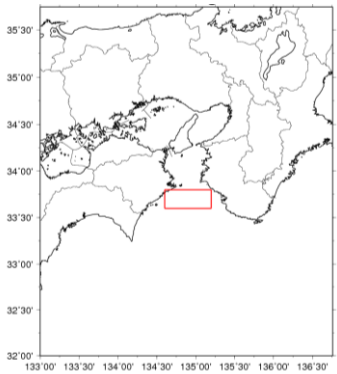

Fig. 23 the calculation region of convergence.

As is expected, the convergence of the region got stronger under more stable conditions, as shown in Table 2. Above all, the convergence was strong at 02:00~03:00 and 03:00~04:00 JST when the amplifying and slimming of water vapor flux can be seen clearly. Accordingly, under more stable conditions, the flow along the terrain gets stronger and the flow gathers more towards the center of the Kii channel.

In addition, in the same region, the average vertical velocity under about 6000 m was checked. As a result, there was a tendency that the vertical velocity of the more stable conditions to be larger, as shown in Table 2. Therefore, the increase in flow along the topography is considered to have strengthened the convergence and enhanced the vertical flow to escape upward. This change in flow can be seen as the amplifying of water vapor, as is displayed in Fig. 20.

Furthermore, the average *v*-component velocity was investigated around the inlet of the Kii channel up to around 6000 m. Consequently, the general tendency that the *v*-velocity gradually became larger under more stable conditions can be seen even though the difference was just a little, as shown in Table 3. This also indicates that the flow inflowing to the Kii channel gets stronger and tends to enter the deeper side of the channel under more stable conditions.

Table 3 the average value from 3:00 to 4:00 of convergence in the x-direction, v-velocity, and w-velocity in the region of Fig. 5

	Exp (Rep)	Exp (2)	Exp (4)
convergence	-0.8088	-0.3769	0.2605
***v*-velocity**	8.3106	8.3827	8.8623
***w*-velocity**	-0.0673	0.0281	0.1444

(3) Summary of Verification

In summary, it is apparent that atmospheric stability has an impact on defining the inflow of water vapor into the land area. Under more stable conditions, air mass tends to go around mountains instead of going over them, hence, the air current along the terrain gets stronger. Owing to such a mechanism, it becomes easier for the water vapor flow to gather towards the center of the channel, thus the area showing the large water vapor flux becomes thinner and higher, and reaches middle levels (2000~5000 m). Thus, the hypothesis is proven.

3.4 Influences of increment of water vapor itself on the water vapor inflow captured by the Pseudo Global Warming Experiment

Although the influence of atmospheric stability on the inflow of water vapor has been discussed so far and it revealed that stability has an impact on the water vapor inflow, it has not yet been discussed whether the increase in the amount of water vapor itself affects the way water vapor flows in. To assess the effects of increased water vapor, the comparisons are performed using the existing data of the Pseudo Global Warming experiment which has a stable

environment with more water vapor. In this paper, the influence of stability is mainly focused on, therefore, the sensitivity experiment that changes the conditions of water vapor only is not implemented.

(1) Configuration of Pseudo Global Warming Experiment

In the paper, the previous result of the Pseudo-Global Warming (PGW) experiment conducted by Osakada (Osakada and Nakakita, 2020) is utilized to investigate the difference. The PGW experiments can simulate meteorological phenomena in a global warming environment by assigning the global warming difference such as temperature and water vapor to the initial and boundary conditions of simulation experiments. The result of MRI-AGCM3.2S (Mizuta et.al, 2012) is used as the global warming difference. MRI-AGCM3.2S is based on RCP8.5 which simulates a scenario in which the average global surface temperature increases by about 4 ℃. In addition, MRI-AGCM3.2S is an ensembled simulation using four SST (abbreviated from Sea Surface Temperature) distributions: the three SST distributions (c1~c3) from the CMIP5 (Coupled Model Intercomparison Project) forecast and the SST distribution (c0) averaged over other distribution (c1~c3). In this PGW experiment, c0 was given as the global warming difference. The other setting such as the range, spatial resolution, and calculation time is the same as the reproductive experiment. The lapse rate for the profile of potential temperature which reflects the magnitude of atmospheric stability in the PGW experiment is $d\theta/dz = 0.0051436$ calculated in the same way listed in Table 2. PGW experiment has a close but little higher value of lapse rate than the one of Exp (4). Thus, the PGW of RCP8.5 is approximated this time as Exp (4) plus the effect of increased water vapor content.

(2) Influences of increment of water vapor itself on water vapor inflow and its balance with atmospheric stability

The results of the reproductive experiment, sensitivity experiments, and PGW experiment are compared in terms of rainfall and water vapor flux to discuss not only the change in atmospheric stability but also the increase in water vapor itself.

(a) Differences in the inflow of water vapor flux

First of all, as discussed in the last section, in the sensitivity experiments under more stable conditions, there are vertical amplifications of the low-level pool of water vapor flux because of the larger convergence around the inlet of Kii channel. Compared to sensitivity experiments, the low-level pool of water vapor flux in the PGW experiment gets stronger and reaches higher altitudes than in any other case at any time, as shown in Fig. 24 and Fig. 25.

Next, the total amount of water vapor inflow flux through the east-south vertical cross-sections around the Kii channel is compared. The sum of all the inflow of water vapor flux is calculated by adding the whole amount of inflow into the vertical cross-section in the region of Fig. 26. As summarized in Table 4, the results indicate that, in the sensitivity experiments under more stable conditions, the total amount of water vapor flux gradually became larger. This trend that the inflow amount of water vapor flux becomes larger under the more stable conditions could be due to the larger convergence in the more stable conditions. Compared to such the result, in the PGW experiment, the total amount of water vapor flux became much higher than in any other case all the time. Thus, there is a dramatic increment in the quantity of water vapor inflow flux into the heavy rainfall area in the future. Since such a large

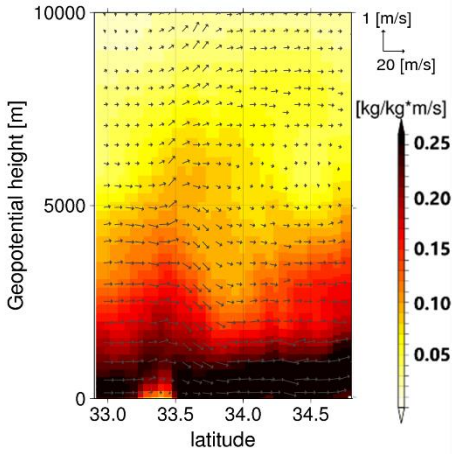

Fig. 24 Three-dimensional distribution of water vapor flux (shade) from 3:00 to 4:00 in the south-north vertical cross-section of the region framed in red in Fig.19 (x: latitude, y: altitude) and wind velocities (arrows) in PGW.

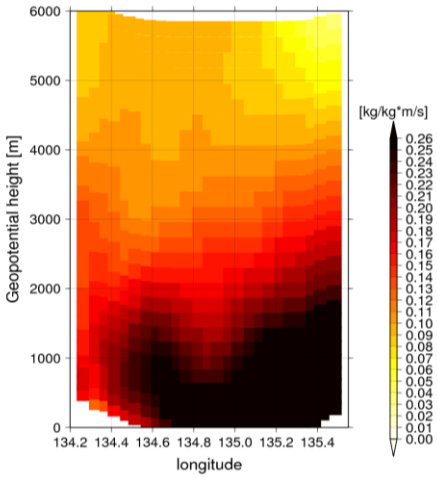

Fig. 25 Three-dimensional distribution of averaged water vapor flux (shade) from 3:00 to 4:00 in the west-east vertical cross-section of the region framed in blue in Fig. 19 (*x*: longitude, *y*: altitude) in PGW experiments. Arrows correspond to wind velocity.

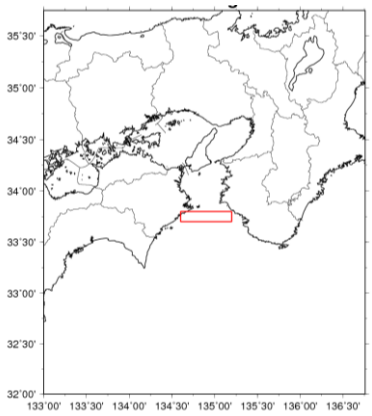

Fig. 26 Setting range for calculating the total amount of water vapor flux inflowing into the Kii channel.

Table 4 Total amount of water vapor flux inflowing to the cross-section of Fig. 26.

Time	Exp (Rep)	Exp (2)	Exp (4)	PGW Exp
11-12	68.06	69.39	70.89	89.59
00-01	72.57	73.51	74.99	91.15
01-02	73.00	75.59	79.44	89.77
02-03	80.47	84.18	88.86	98.81
03-04	87.20	91.60	96.77	111.56
04-05	89.73	89.94	93.21	113.63
05-06	84.29	85.64	88.82	106.73

increment of the total water vapor flux found in the PGW experiment was not discovered in the Exp (4) which is under atmospheric stability similar to that of the PGW experiment, this large increment of water vapor flux can be mainly caused by the increment of water vapor mixing ratio, which holds a huge difference between the PGW experiment and Exp (4), caused by global warming.

Thus, while the increase in water vapor itself has a large impact on the total water vapor inflow, the total inflow is also affected by differences in atmospheric stability.

(b) Differences in how it rained

Next, how it rained is compared while taking into account differences in atmospheric stability and water vapor mixing ratio.

In the reproductive experiment and all sensitivity experiments, back-building convective systems occurred and produced heavy rainfall, as illustrated in Fig. 27. The time to start raining did not vary with the atmospheric stability conditions, however, the amount of precipitation of the convective systems differed among the experiments. To highlight the difference, the differences in accumulated rainfall of each sensitivity experiment from the reproductive experiment are shown in Fig. 28. From those figures, in the more stable conditions, although there were some places where rain got heavier, the rain was getting decreased as a whole convective system. Accordingly, even though the amount of water vapor inflow increased to some extent in more stable conditions as mentioned, the amount of rainfall decreased. This implies that the localized rainfall got weakened due to the enhanced stability at the site, that is, the effectiveness of high stability exceeded that of the amount of water vapor which increased a little so that it rained weaker in the sensitivity experiments.

However, in the PGW experiment, even though the atmosphere was as stable as the Exp (4), it rained heavier and more intense as shown in Fig. 29. As shown in Fig. 28, by taking the difference in rainfall in the PGW experiment from that of the reproductive experiment, it is clear that there was no decrease of rainfall around the heavy rainfall area unlike the stable sensitivity cases, but huge increase around Kameoka. Therefore, the back-building convective

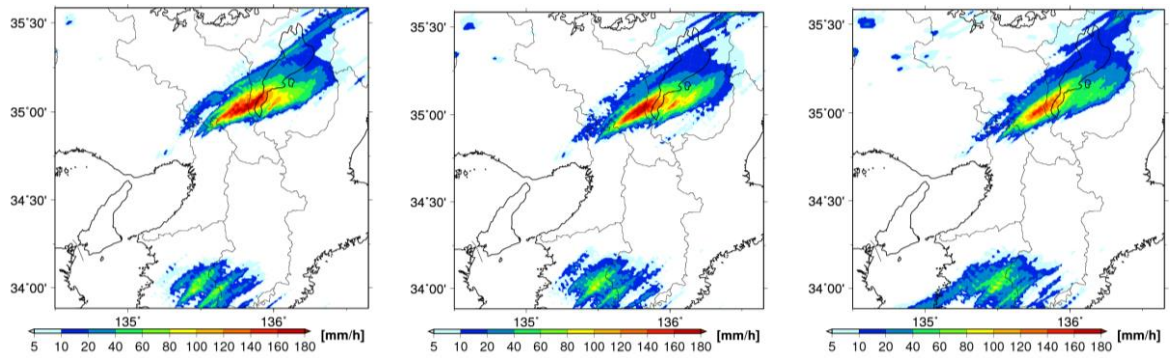

Exp (Rep) **Exp (2)** **Exp (4)**

Fig. 27 Accumulation of rainfall from 00:00 to 06:00 on July 15th in each experiment.

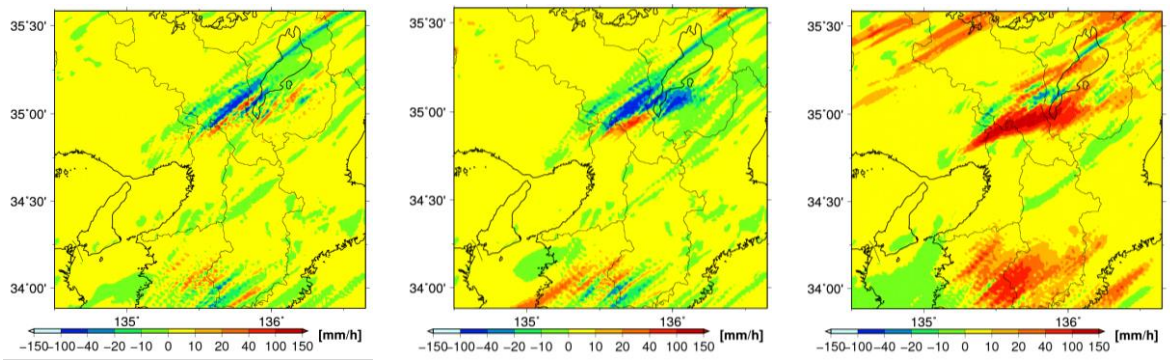

Exp (2)- Exp (Rep) **Exp (4)- Exp (Rep)** **PGW exp- Exp (Rep)**

Fig. 28 Difference of accumulation rainfall between each experiment and reproductive experiment.

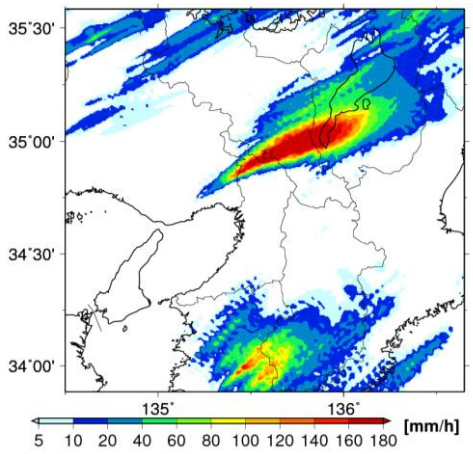

Fig. 29 Accumulation of rainfall from 00:00 to 06:00 on July 15th in PGW experiment.

system in Kameoka is proved to be a more terrible disaster in a warming climate. This result implies that the rainfall got heavier due to the much-increased amount of water vapor flux caused by the increment of water vapor mixing ratio, even though the atmospheric stability is high. That is, the effectiveness of the huge increased amount of water vapor overwhelmed the higher atmospheric stability to increase rainfall in the PGW experiment.

Thus, a large increase in the amount of water vapor inflow could significantly contribute to the enhancement of rainfall amount in the future.

3.5 Conclusion of Chapter 3

Through the sensitivity experiments with more stable atmospheric stability conditions, atmospheric stability was found to affect the inflow of water vapor along the topography in the meso-α~β-scale, which was the focus of the study. It appears that the amplifying and slimming of large water vapor flux can happen since the stronger convergence is caused around the channel by the stronger flow along with the terrain under more stable conditions. In addition, the amount of water vapor inflow flux gradually increases under more stable conditions. Furthermore, the result suggests that the enhancement of rainfall in the future could be mainly caused by the increase in water vapor inflow.

Besides, because atmospheric stability is getting higher due to global warming, if such amplifying and slimming of water vapor flux seen in stable

conditions can be captured as a trend in the world of global warming, it could serve as an indicator of the progress of global warming.

In future works, to deeply understand the mechanism, should be to investigate whether the same effect happens in other areas, how atmospheric stability relates to the rainfall, and how the flow of water vapor is changed by an increase of water vapor itself. Moreover, it is needed to investigate what balance between the water vapor increment and high stability causes heavy rainfall by utilizing sensitivity experiments.

4. SOM analysis for verifying the validity of the Result of Sensitivity experiments

To corroborate the results of the sensitivity experiments utilizing the numerical simulation of the model CReSS and to verify whether the influence of stability on water vapor flow can actually happen or not, the cluster classification was carried out by applying Self-Organizing Map (SOM) to the MSM analysis data which represents an atmospheric field that has actually occurred in the real world. Although MSM analysis data is also the model representation, it is assimilated with the real observation and forecast, thus it is treated as a more realistic one.

4.1 SOM method and settings of input

SOM is an unsupervised learning neural network constructed with input and output layers, and SOM map can express the representative characteristics of input vectors by learning repeatedly (Kohonen, 1998). Moreover, the nodes which are close to each other in position in the SOM map have similar characteristics, while the nodes which are farther away from each other have different characteristics. The SOM has been utilized and applied for Meteorological analysis in some previous studies (Nakakita and Osakada, 2018) to classify atmospheric conditions.

The algorithm of SOM is operated by the following four steps.

1) Give the initial vectors randomly chosen to all reference vectors $\boldsymbol{mi}$ of competitive layer nodes i in the map.
2) Compare the input vectors $\boldsymbol{x}$ to each reference vector $\boldsymbol{mi}$ of nodes, subsequently find the node where Euclid distance is minimum.
3) Modify reference vectors $\boldsymbol{mi}$ of the node selected in step 2 and reference vectors $\boldsymbol{mi}$ of nodes in the vicinity of the selected node to make it a little more similar to the input vectors by using the neighborhood function hci.
4) Repeat the steps 2 and 3.

Through this procedure, eventually, the reference vectors $\boldsymbol{mi}$ of each node of the SOM map can express the representative characteristics of input vectors.

Modification of reference vectors $\boldsymbol{mi}$ is performed by the following calculations with neighborhood function hci.

$$m_i(t+1) = m_i(t) + h_{ci}(t, \|r_c - r_i\|)[x - m_i(t)], \quad (5)$$

$$h_{ci}(t, \|r_c - r_i\|) = \alpha(t) \cdot \exp\left[-\frac{\|r_c - r_i\|^2}{2\sigma^2(t)}\right], \quad (6)$$

where, t is the number of learning iteration, r_c corresponds to the position vectors of the node chosen in step 2, and r_i shows the position vectors of the arbitrary node. α is the coefficient number of learning rate ($0 < \alpha < 1$) and σ is the neighborhood radius which indicates the radius of the node sets modified by the neighborhood function. α and σ are set with the total number of learning T to become smaller and smaller with t as the following equations.

$$\alpha(t) = \alpha(0)\frac{T - t}{T}, \quad (7)$$

$$\sigma(t+1) = 1 + (\sigma(t) - 1)\frac{T - t}{T}. \quad (8)$$

From the above characteristics of the neighborhood function, the reference vector of the node closer to the winner node (the best matching node, that is, node c) is modified more, and the degree of modification becomes smaller with t. In this research, $\alpha(0)$ was set as 0.2, $\sigma(0)$ was set as 0.5, T was set as 1000, and the number of nodes was set to be 10×10, therefore, the two-dimensional SOM map which had 100 nodes was generated.

Using this algorithm, actual historical data obtained by MSM was classified. To investigate whether a similar case to the result of the CReSS

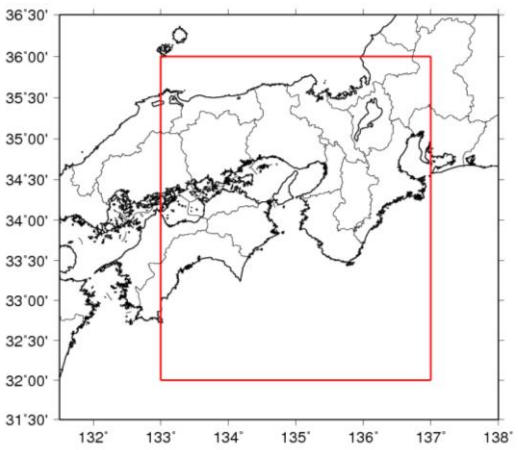

Fig. 30 Configuration area.

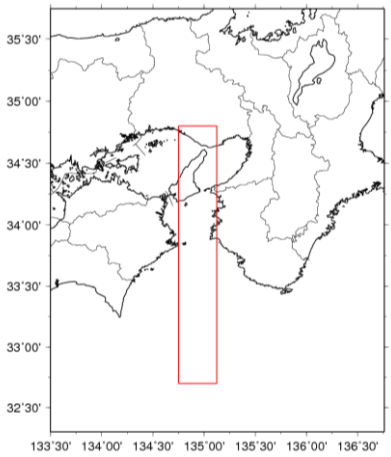

Fig. 31 Configuration area.

sensitivity experiments exists in the actual case, the MSM analysis values from July 1st to August 31st UTC (stands for Coordinated Universal Time) were used. In addition, the data from 2010 to 2021was used. The MSM analysis data can be obtained every 3 hours, therefore, a total of 8832 data counts were used for this SOM analysis.

Among the MSM analysis data, five variables were picked up and used as the vectors used in the SOM classification. Firstly, the analysis area that extends to the south of the Kii channel was set as illustrated in Fig. 30 (32~36°N and 133~137°E) in a region with 65×81 meshes. Additionally, another area that enters the Kii channel was set as shown in Fig. 31 (32.7~34.8° N and 134.75~135.125°E) in a region with 12×22 meshes. Five variables were chosen to characterize the atmospheric field at each time and to characterize how much water vapor inflowed into the area of Kii channel at each time. The five variables used include

1) Surface water vapor mixing ratio q_v in the range of Fig. 30.
2) Surface horizontal wind speed u in the range of Fig. 30.
3) Surface horizontal wind speed v in the range of Fig. 30.
4) Vertical profile of temperature averaged in the range of Fig. 30.
5) South-north vertical cross-section's water vapor inflow flux along the range of Fig. 31. (values calculated in the same way as 2.3 (2) and averaged).

By the first three variables, the surface horizontal distribution of water vapor flux can be expressed and used as an indicator of classification for the degree of inflow from the south to the land area. The fourth variable can represent the strength of atmospheric stability around the channel. Lastly, the fifth variable can express how water vapor flux inflowed vertically into the channel in the past cases. These variables are used to classify the data to see if the relationship between the way water vapor flows into the atmosphere and atmospheric stability seen in the sensitivity experiment is also seen in actual real-world values.

4.2 Results of SOM classification

By using the algorithm of SOM, the past 8832 cases were classified onto 10×10 nodes to represent their characteristics. Please refer Fig. 35, 36 and 37 in the appendix for all detail results of each classified nodes in SOM map.

To know the magnitude of atmospheric stability condition, the gradient of the potential temperature in each node is calculated by

$$\frac{d\theta}{dp} = \frac{\theta_{500hPa} - \theta_{1000hPa}}{500hPa - 1000hPa}, \tag{9}$$

and the value of each node in SOM map is shown in Fig. 32, and the smaller value is corresponding to a more stable condition.

Hereinafter, the node position is called (i,j) and the figures are arranged like a matrix. Moreover, the number of data that are classified on each node is counted and shown in Fig. 33.

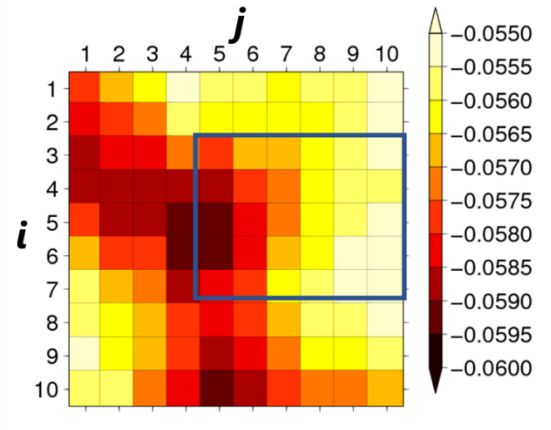

Fig. 32 Lapse rate of the potential temperature in each node. The nodes enclosed by the blue frame correspond to the nodes extracted under the conditions of a meteorological field where water vapor flux from the south is predominant through the Kii channel .

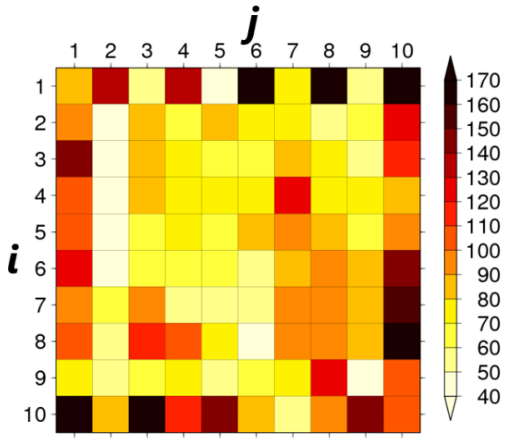

Fig. 33 Number of data classified to each node in SOM map (Vertical axis shows i, horizontal axis shows j).

The classification was conducted well, for example, the cases of before, during and after Kameoka rainfall were classified as the node of (5,8), in which the flow from the south is dominant and the low-level large water vapor flux flowed into the channel.

Based on the result of the classification, among all the nodes, only the nodes in which the south inflow is dominant and strong, are focused on and extracted by checking both the surface wind and the amount of water vapor flux at low-level into the Kii channel. By such extraction, the nodes of ($i \in [3,7]$, $j \in [5,10]$) are discussed in the study. The reference vectors of these extracted nodes are also shown in Fig. 38, 39 and 40 in Appendix.

By this procedure, it shows that the nodes with a small value of the gradient, which means a condition of stable atmosphere, such as the node where i= 4 or 5 or 6 and j=4 or 5 as shown in Fig. 34, have the characteristic that a large water vapor flux is confirmed in not only the low-level but also in the middle-level (at the level of 600 and 700hPa) as shown in Fig. 34. On the contrary, it can be found middle-level strong water vapor flux in the other nodes. This reflects that there exists the tendency that the large water vapor flux in the middle-level can be seen only in the nodes with higher stability conditions. This tendency is consistent with the result of the sensitivity experiments in the last chapter. In addition, as seen in Fig. 33, the number of past data classified in such nodes is not small. Therefore, a such phenomenon that the altitude of large water vapor flux is increased in stable conditions is not rare, and can often happen in the

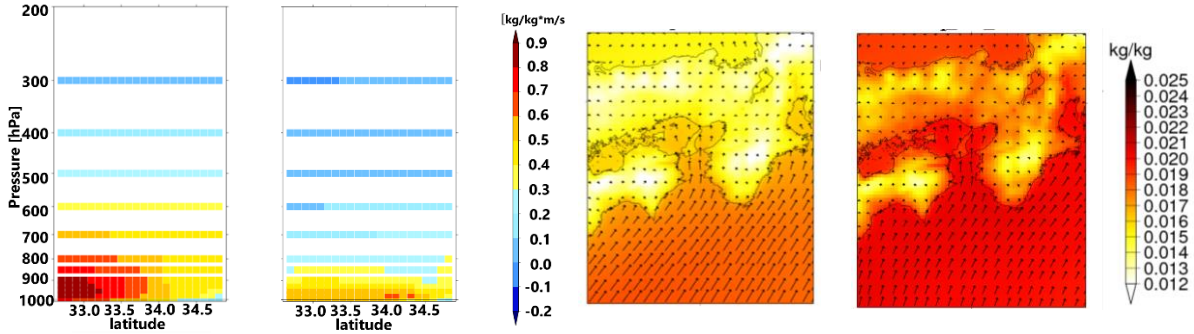

(a) Node (5,5) (b) Node (5,10) (a) Node (5,5) (b) Node (5,10)

Fig. 34 Comparison of the water vapor flux in south-north vertical cross-section along Kii channel between the nodes with predominant inflow from the south and different degrees of stability. The right figures show the spatial distribution of water vapor mixing ratio (color shade) and wind vectors (arrows) at the surface at those nodes used in extracting the nodes.

real world.

4.3 Conclusion of the Chapter

By applying the SOM clustering classification to the MSM analysis data, the validity of the results of the CReSS sensitivity experiments was confirmed. As clarified by the sensitivity experiments, stability conditions can influence the water vapor inflow along the terrain, such that water vapor inflow is gradually getting amplified under more stable conditions, and such tendency can be confirmed in the real world, even though it was the verification conducted on a wide spatial scale that can be captured in MSM and the verification that rough representative features were captured by SOM.

5. Conclusion

In the study, it was focused that how water vapor, which is necessitated for the Baiu heavy rainfall to occur and be maintained, inflows into the heavy

rainfall area along the terrain in the meso-α~β -scale, that is to say, the water vapor inflow path was focused. In addition, the hypothesis that atmospheric stability would influence the way of water vapor inflowing was formed.

Accordingly, through the analysis, the following things were elucidated in the study;

I Water vapor inflow paths along the terrain into the rainfall area can be confirmed in some past heavy rainfall events and water vapor flux and CAPE visually reveal it well, and the vertical flow of water vapor flux is important as well as the horizontal distribution of water vapor flux.

II Atmospheric stability has an impact on the water vapor inflow path near land areas. In detail, under more stable conditions, the flow of water vapor becomes thinner and higher due to the stronger convergence towards the center of the channel caused by the stronger flow along topography. Moreover, under more stable conditions, the total amount of water vapor flux gradually became larger.

As future works, it is needed to understand why CAPE can visually reveal the water vapor path clearly by considering the water vapor and the temperature profile together. Besides, a sensitivity experiment in which the water vapor mixing ratio is changed should be conducted to confirm how the change of water vapor mixing ratio itself influences the water vapor inflow path to the heavy rainfall area. Lastly, it is needed to reveal the relationship between the changes in inflow of meso-α~β-scale and changes in rainfall of meso-γ-scale. In addition, to deepen our understanding of how water vapor travels through the terrain and to investigate whether stable conditions of global warming form a new water vapor path, the analysis along more small topographic features, such as valleys in mountainous regions, should be conducted.

Even though the same relative humidity was given as the water vapor setting through the Kameoka sensitivity experiments in this research, the conclusion that the inflow of water vapor to the Kii channel becomes larger as the stability increases remains the same. However, since some ambiguities remain, an experiment in which water vapor is given as a constant water vapor mixing ratio or an ideal experiment in which only wind flow will be conducted and analyzed as future works.

References

横田寛伸 (1992): 淀川チャンネル型大雨の比較解析，日本気象学会関西支部年会講演予稿集，pp.14-48.

Hibino, K., Takayabu, I., Wakazuki, Y., Ogata, T. (2018): Physical Responses of Convective Heavy Rainfall to Future Warming Condition: Case Study of the Hiroshima Event, frontiers in Earth Science, Vol.6, Article 35.

Kohonen, T. (1998): The self-organizing map, Neurocomputing, Vol.21, pp.1-6.

Nakakita, E., Tsutsui, M., Ikebuchi, S., Takasao, T. (1998): Analysis of Rainfall Distribution based on Mesoscale Dynamic Models, Proceedings of the Japanese Conference on Hydraulics, Vol.32, pp.13-18.

Nakakita, E. and Osakada, Y. (2018): Estimation of future changes in the heavy rainfall and atmospheric characteristics in baiu season under climate change, Journal of Japan Society of Civil Engineerings, Hydraulic enginnering, Vol.74, No.4, pp.139-144.

Ninomiya, K. (1984): Characteristics of Baiu Front as a Predominant Subtropical Front in the Summer Northern Hemisphere, Journal of the eteorological

Society of Japan, Vol.62, No.6, 880-894.
Osakada, Y. and Nakakita, E. (2020): Multi-scale analysis on pseudo global warming experiment for back-building rainfall based on different resolutions, Journal of Society of Civil Engineerings, Hydraulic engineering, Vol.76, No.2, pp1-6.

Appendix

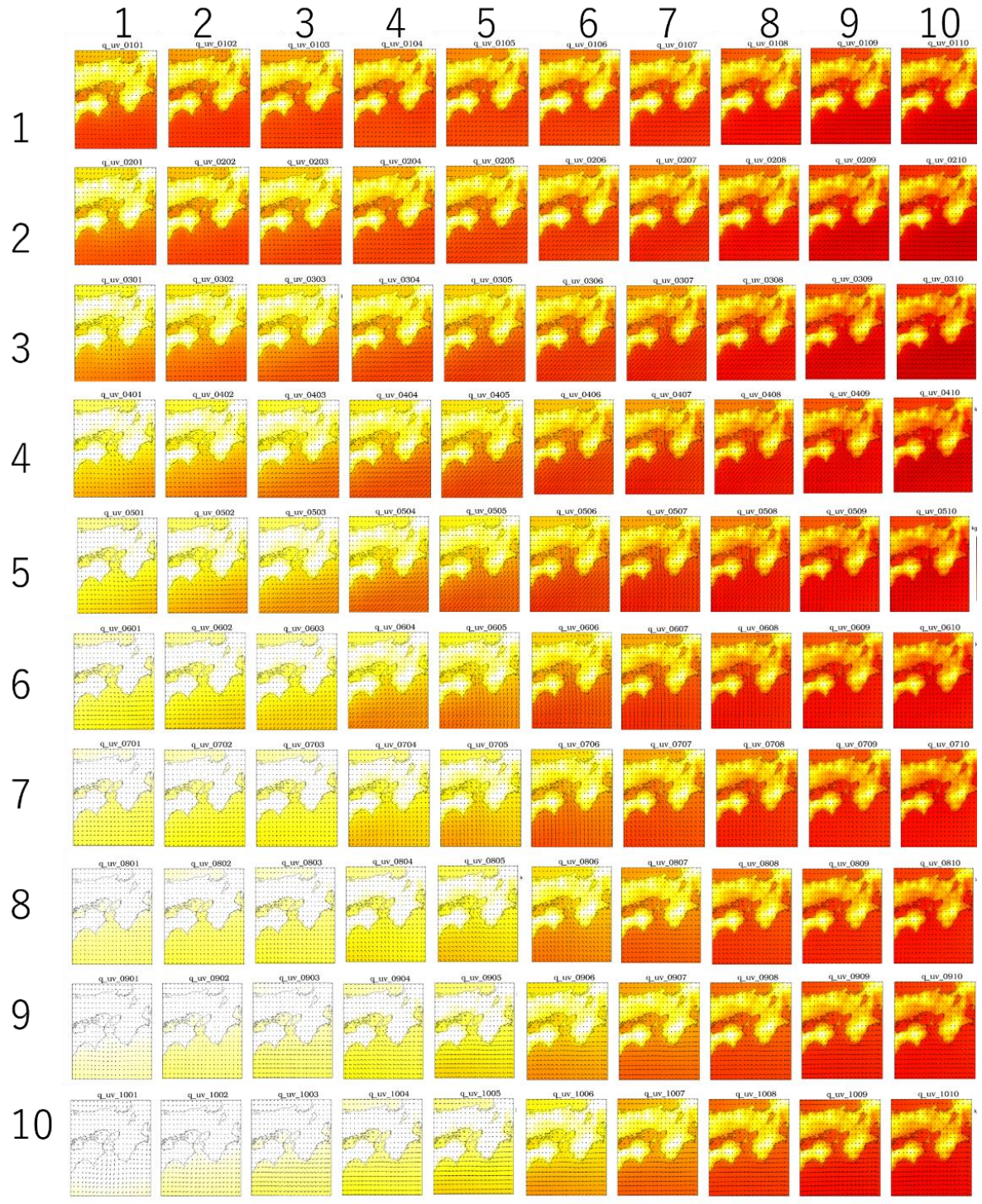

Fig. 35 Wind vectors and the water vapor mixing ratio in each node (vertical axis shows *i*, horizontal shows *j*.)

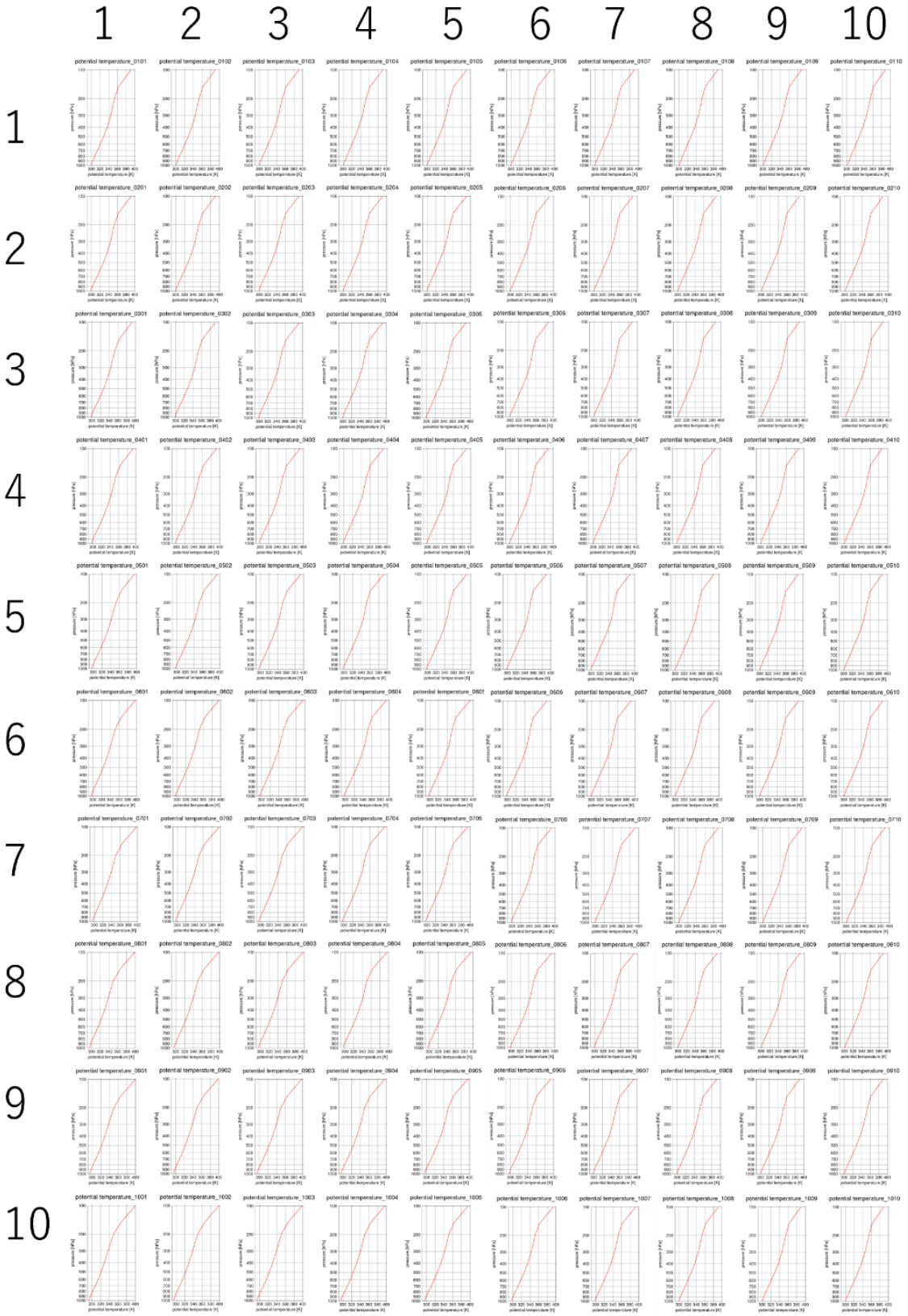

Fig. 36 Vertical profile of the potential temperature in each node (Vertical axis shows i, horizontal axis shows j).

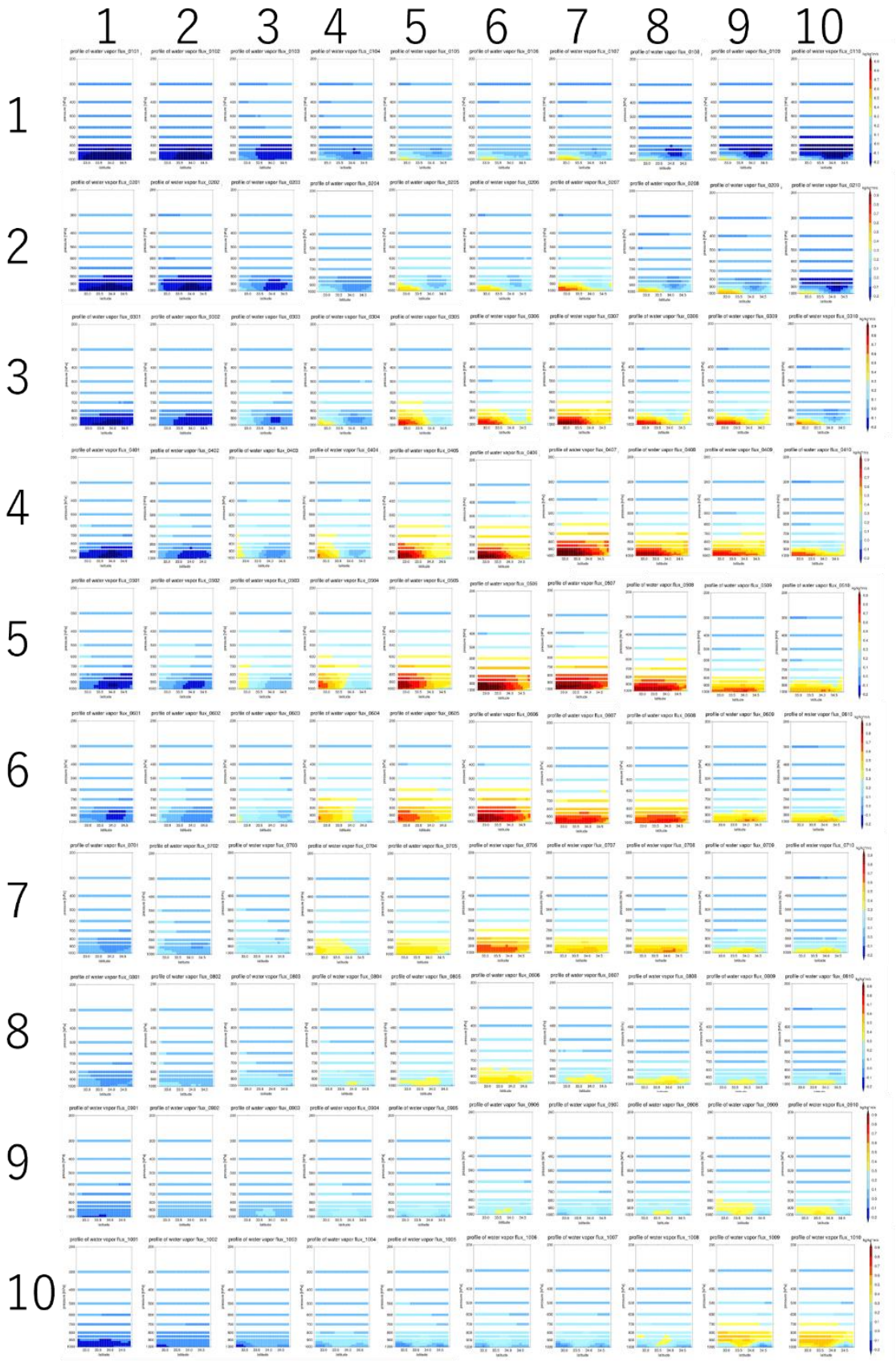

Fig. 37 South-north vertical cross-section showing the water vapor flux into the channel in each node. (Vertical axis shows i, horizontal axis shows j).

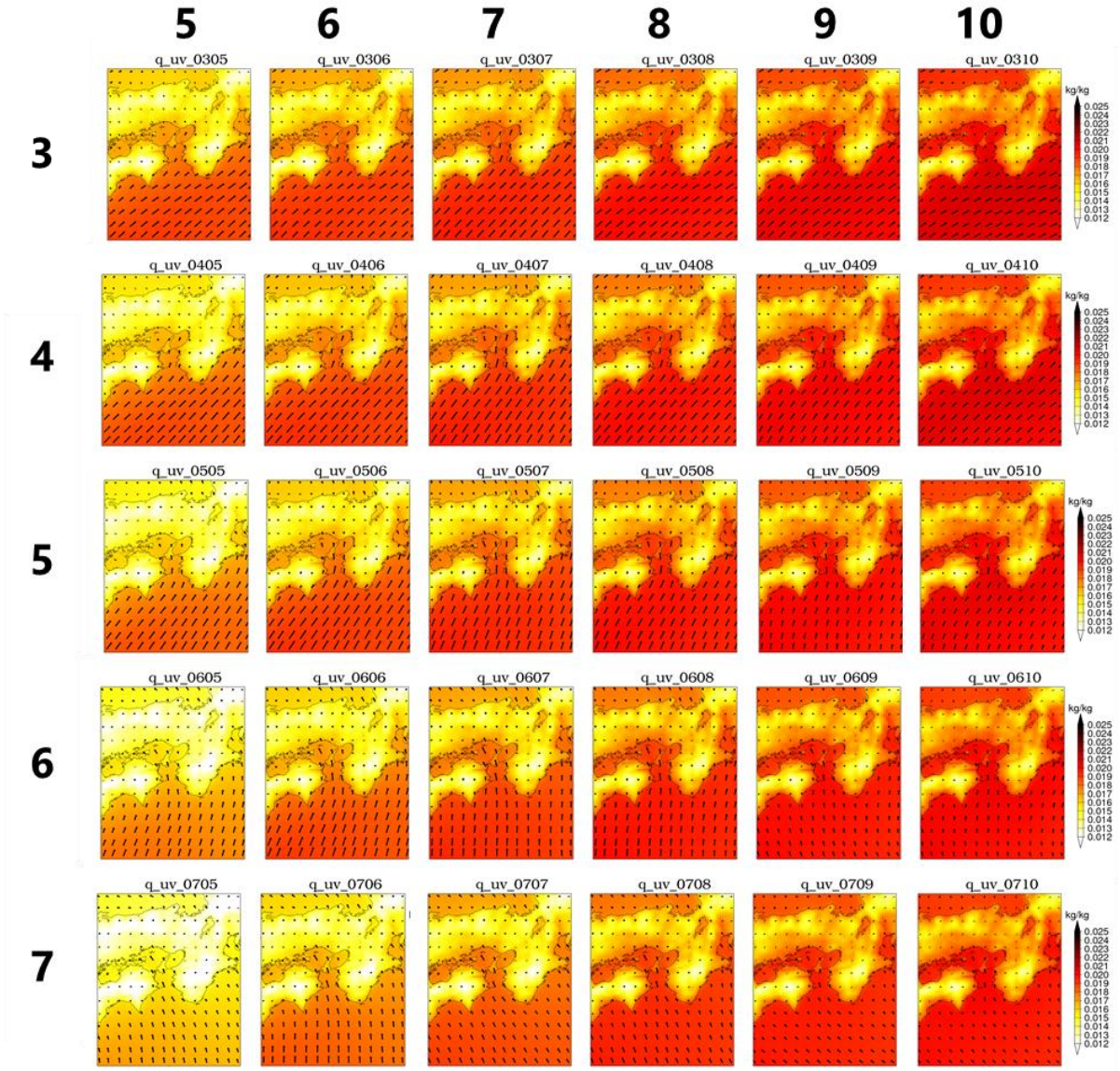

Fig. 38 Surface winds and the surface water vapor mixing ratio of the extracted nodes (Vertical axis shows i, horizontal axis shows j). Shade represents surface water vapor mixing ratio and arrows show surface wind vectors.

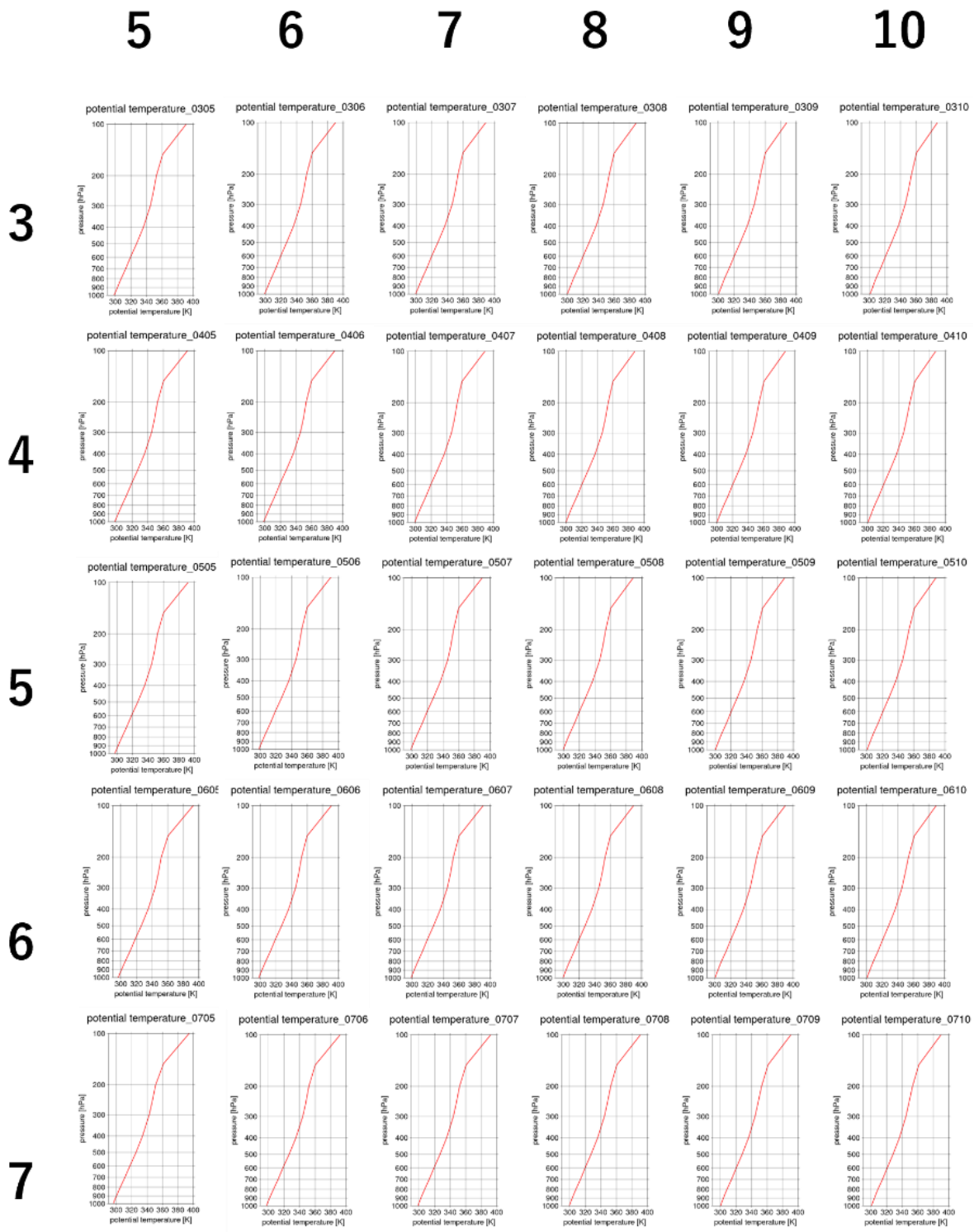

Fig. 39 Profile of the potential temperature of the extracted nodes.

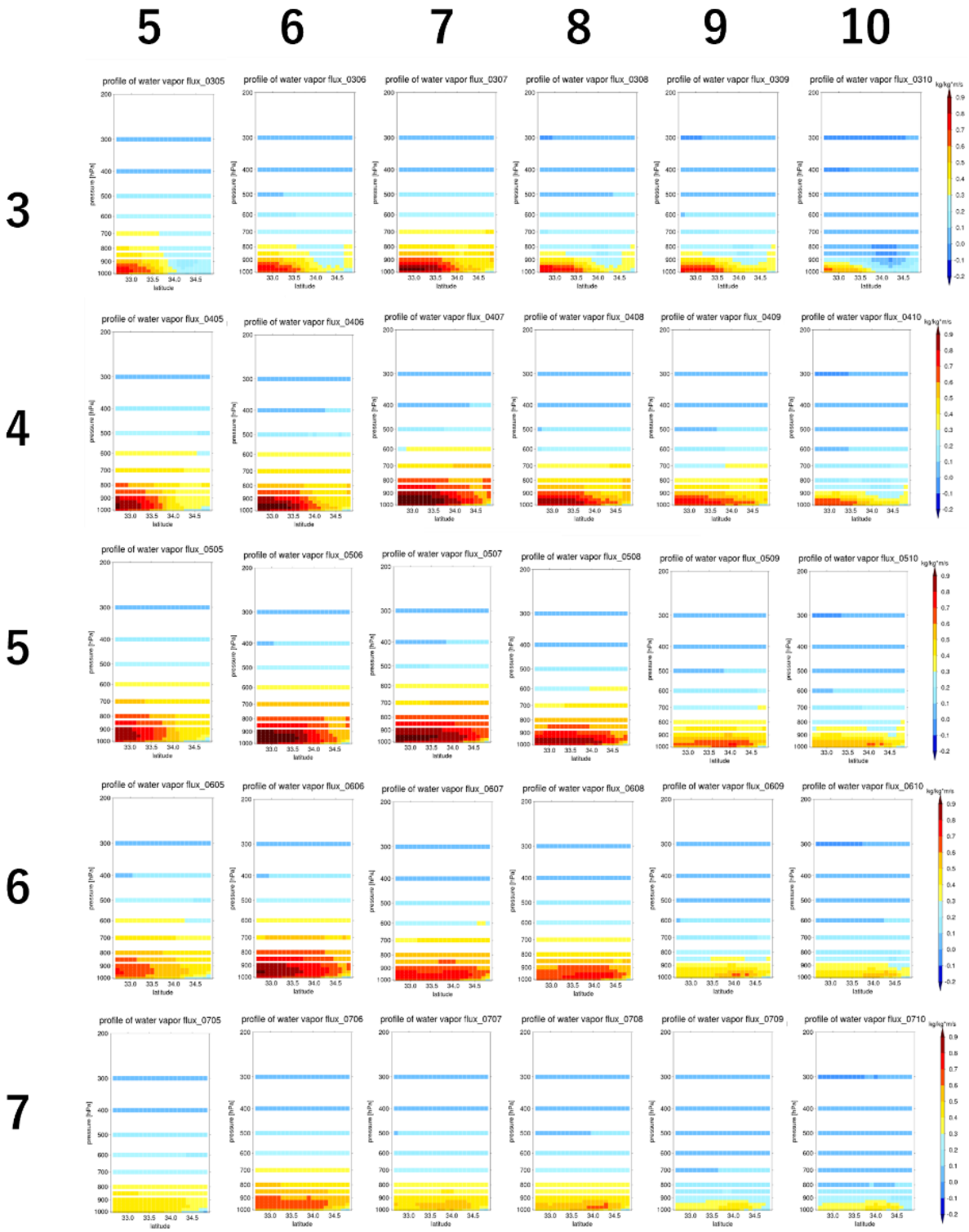

Fig. 40 South-north vertical cross-section showing the water vapor flux into the channel in the extracted nodes. (Vertical axis shows i, horizontal axis shows j).

(Received August 27, 2022)